

Chimeras in leaky integrate-and-fire neural networks: effects of reflecting connectivities

Nefeli Dimitra Tsigkri-DeSmedt^{1,2}, Johanne Hizanidis^{1,3}, Ekehard Schöll⁴, Philipp Hövel^{4,5}, and Astero Provata^{1,a}

¹ Institute of Nanoscience and Nanotechnology, National Center for Scientific Research “Demokritos”, 15310 Athens, Greece

² Section of Solid State Physics, Department of Physics, National and Kapodistrian University of Athens, Athens, Greece

³ Crete Center for Quantum Complexity and Nanotechnology, Department of Physics, University of Crete, 71003 Heraklion, Greece

⁴ Institut für Theoretische Physik, Technische Universität Berlin, Hardenbergstraße 36, 10623 Berlin, Germany

⁵ Bernstein Center for Computational Neuroscience Berlin, Humboldt-Universität zu Berlin, Philippstraße 13, 10115 Berlin, Germany

Received 18 March 2017 / Received in final form 22 May 2017

Published online 24 July 2017 – © EDP Sciences, Società Italiana di Fisica, Springer-Verlag 2017

Abstract. The effects of attracting-nonlocal and reflecting connectivity are investigated in coupled Leaky Integrate-and-Fire (LIF) elements, which model the exchange of electrical signals between neurons. Earlier investigations have demonstrated that repulsive-nonlocal and hierarchical network connectivity can induce complex synchronization patterns and chimera states in systems of coupled oscillators. In the LIF system we show that if the elements are nonlocally linked with positive diffusive coupling on a ring network, the system splits into a number of alternating domains. Half of these domains contain elements whose potential stays near the threshold and they are interrupted by active domains where the elements perform regular LIF oscillations. The active domains travel along the ring with constant velocity, depending on the system parameters. When we introduce reflecting coupling in LIF networks unexpected complex spatio-temporal structures arise. For relatively extensive ranges of parameter values, the system splits into two coexisting domains: one where all elements stay near the threshold and one where incoherent states develop, characterized by multi-leveled mean phase velocity profiles.

1 Introduction

Chimera states, which are characterized by spatial coexistence of coherent and incoherent oscillators, appear in systems of nonlocally coupled oscillators and in oscillator networks with complex connectivity [1–3]. Their most striking feature is that all oscillators belonging to the coherent parts have equal mean phase velocities, while the incoherent parts demonstrate a variable mean-phase-velocity profile, often taking the shape of an arc [3,4]. A wide range of oscillatory models exhibit chimera states many of which come from the domain of neuroscience [5–14].

Basic open questions related to the collective properties of oscillator networks are: (a) how does the network connectivity influence the final synchronization state? (b) Which connectivity patterns induce chimera states? (c) How is the chimera multiplicity affected by the interplay of dynamics and connectivity? Along these lines of research, we compare here two kinds of connectivity patterns, nonlocal and reflecting, in networks of the Leaky

Integrate-and-Fire (LIF) elements [15]. We locate the parameter regions where chimera states are observed in either case and we investigate the influence of the network connectivity on the final states.

Chimera states have been studied in the literature using a variety of coupling topologies. Initially, chimeras were extensively investigated for symmetric nonlocal coupling schemes [1,2,7]. In more recent studies they were found in a variety of coupling geometries and oscillatory dynamics. In references [9,16–20] it was shown that the composite effects of nontrivial connectivity together with the nonlinearity of the dynamics lead to multi-chimeras and chimera death states. Asymmetric nonlocal coupling has been proposed to control the undesired erratic lateral motion of chimeras [21]. Hierarchical (fractal) connectivity schemes have given rise to the pattern of nested chimeras, which appears in systems of hierarchically arranged neural oscillators [10], reactive units [22] and coupled Van der Pol oscillators [23]. Other nonlocal coupling schemes where complex chimera patterns have been reported include modular networks consisting of several communities [11], 2D (square lattice) and 3D (cubic lattice) connectivities [24–26].

^a e-mail: a.provata@inn.demokritos.gr

The LIF dynamical system used in this study is one of the classical models describing single neuron activity [15]. **The interplay between neuron dynamics and network topology is a non-trivial problem in neuroscience, given that the human brain consists of approximately 10^{10} neurons, each of which is linked with up to 10^4 other ones via synapses.** Today's advanced Magnetic Resonance Imaging (MRI) and functional Magnetic Resonance Imaging (fMRI) equipment are revealing detailed connectivity patterns, which is a subject of intense international research, both experimentally and computationally [27–31]. In [32] in particular, Finn et al. proposed that it is even possible to identify a person from the “fingerprints” of their brain connectivity patterns, as mapped by fMRI. In that reference the authors depict intricate network connectivity profiles extracted from human brain recordings. Two specific cases are discussed: (a) diagonal connectivity, i.e., connection edges exist between regions in one hemisphere and regions in the other hemisphere, arranged diagonally opposite to each other and (b) reflecting connectivity, i.e., the connectivity edges which link the two hemispheres are all perpendicular to the plane separating them. These experimental observations have inspired us to implement reflecting connectivity in our LIF networks and to study the implications of this complex scheme in terms of synchronization properties and chimera states. The case of diagonal connectivity is outside the scope of the current work and is left for future studies.

Chimeras may be related to various neurological states such as the phenomenon of unihemispheric sleep observed in animals [33,34], or the onset of epilepsy [12]. In addition, chimera states might be relevant in cognition, as collective neural response to an external stimulus can be understood as a pattern. One might hypothesize that each synchronization pattern describes a “memory” (or any cognitive activity) and can be recalled and reproduced later if a similar electrical signal arrives. Once the connectivity is established and remains unchanged in time, the same stimulus will create the same synchronization effect in the neurons involved and this corresponds to recalling a “memory” pattern. This approach explains why “memories” fade away with time: once enough of the synapses break or neurons die (due to aging, disease, or accident), it is no longer possible to recreate the synchronization pattern and therefore, to “recall the memory”.

Synchronization properties in nonlocally coupled LIF elements were studied in 2010 by Luccioli and Politi [35] and Olmi et al. [36]. These studies demonstrated the presence of chimera states when a distribution of spiking frequencies is introduced in the dynamics and in cases of symmetrically coupled neuron populations. More recently, synchronization phenomena in the LIF model were explored using negative (repulsive) diffusive coupling with and without refractory period [37,38]. It was shown that for nonlocal coupling, multi-chimera states emerge whose multiplicity (number of coherent/incoherent domains) depends both on the coupling strength and the refractory period. Hierarchical coupling in the LIF model gave rise to nested chimera states and transitions between multi-chimeras of different multiplicities. These results are

indicative of the complexity in synchronization phenomena resulting from the combined effects of the LIF dynamics with different coupling schemes.

In the present manuscript, we consider a ring network consisting of LIF elements coupled via a *positive* diffusive coupling; both nonlocal and reflecting connectivity architectures are discussed. In the nonlocal connectivity each oscillator connects with a number of elements symmetrically arranged around it, whereas in the reflecting connectivity each oscillator is connected with a number of elements arranged in the opposite semi-ring and placed perpendicularly across a standard ring axis (see Sect. 4 for a detailed description). As stated earlier, non-local connectivity has been frequently employed in the literature on chimera states [5–9,12,14], while the idea of reflecting coupling stems from brain studies investigating cases where neurons located on the surface of one hemisphere are connected with neurons arranged on the opposite hemisphere [32]. We also employ a finite refractory period, which is a well established feature of the biological neuron. We give numerical evidence that such network characteristics lead to novel patterns involving multi-leveled incoherent states that coexist with near-threshold elements. These are new interesting spatio-temporal patterns and occur in LIF units when connected via reflecting coupling.

Our work is organized as follows: in Section 2 we recapitulate the main properties of the LIF model and we study synchronization phenomena in coupled LIF elements with positive diffusive coupling, when a finite refractory period is introduced. In Section 3 we scan the parameter space and study the formation of domains with near-threshold elements and clustering phenomena. In Section 4 we consider reflecting connectivity and study the resulting oscillation patterns and transition phenomena. We give evidence of transitions between synchronous oscillations and chimera states with multi-leveled mean phase velocities, using the coupling strength and the refractory period as control parameters. In the concluding section we summarize our main results, we present possible applications and we discuss open problems.

2 Leaky integrate-and-fire model with diffusive coupling and finite refractory period

The LIF model describes the neuron excitation processes and consists of a single linear differential equation accounting for the integration of the neuron potential $u(t)$, followed by an abrupt resetting of the potential to its ground value, or rest state, $u(t) = u_0$ [37]. Namely:

$$\frac{du(t)}{dt} = \mu - u(t) \quad (1a)$$

$$\lim_{\epsilon \rightarrow 0} u(t + \epsilon) \rightarrow u_0, \quad \text{when } u(t) \geq u_{th}. \quad (1b)$$

Equation (1a) represents the integration of the potential $u(t)$, which develops accumulating contributions with rate

Cool.

Credible hypothesis?

μ [39–42]. The term $-u(t)$ on the right hand side of this equation represents the “leaky term” which prohibits the potential from increasing to arbitrarily large values and forces it to converge to the value μ for $t \rightarrow \infty$. An integral constituent of the single LIF model is equation (1b), which restores the potential $u(t)$ to its ground value u_0 every time the potential exceeds its threshold termed as u_{th} . This way a closed potential loop is created with extreme values $u_0 \leq u(t) \leq u_{th}$. Due to the structure of equation (1a), $u(t)$ can reach the value u_{th} and thus drop to the rest state, u_0 , only if $u_{th} < \mu$. Equation (1a) is linear and can be solved analytically as long as the potential $u(t) \leq u_{th}$. The solution is $u(t) = \mu - (\mu - u_0)e^{-t}$ for $u(t) \leq u_{th}$, where, without loss of generality, we have assumed that at $t = 0$ the potential is at the rest state, u_0 . The period T_s of a single LIF oscillation is equal to $T_s = \ln[(\mu - u_0)/(\mu - u_{th})]$.

Biological neurons spend a resting period after firing each spike, which is called “refractory period” p_r . This is an essential feature of spiking neurons and we account for this by adding to the model equation (1) the following condition [37]:

$$u(t) \equiv u_0, \forall t : [l(T_s + p_r) + T_s] \leq t \leq [(l+1)(T_s + p_r)],$$

where $l = 0, 1, 2, \dots$, (2)

i.e., after each firing at times $l(T_s + p_r) + T_s$ the neuron retains its potential to the resting state u_0 for an additional time interval p_r .

Having defined the single element dynamics we proceed by placing a population of identical units on a ring network and connecting them via a nonlocal diffusive coupling. This is the simplest linear coupling and takes the form $[u_j(t) - u_i(t)]$ between elements j and i . The term nonlocal diffusive coupling is used in computational neuroscience to specify the difference (diffusive) coupling, combined with long-distance (nonlocal) connections. As far as the coupling topology is concerned, we will consider two types of connectivity: (a) nonlocal coupling, in Section 3 and (b) reflecting coupling, in Section 4. The topology is defined by the adjacency or connectivity matrix σ_{ij} which is different in cases (a) and (b) as will be discussed in the corresponding sections. For a number of N LIF elements, each of them having potential $u_i(t)$, $i = 1, \dots, N$ and connected in a ring topology, the network dynamics is described by the following scheme:

$$\frac{du_i(t)}{dt} = \mu - u_i(t) + \frac{1}{N_c} \sum_{j=1}^N \sigma_{ij} [u_j(t) - u_i(t)] \quad (3a)$$

$$\lim_{\epsilon \rightarrow 0} u_i(t + \epsilon) \rightarrow u_0, \text{ when } u_i(t) \geq u_{th}, \quad (3b)$$

where N_c is the total number of elements that are linked to each node. We assume that all elements have the same refractory period p_r , threshold potential u_{th} , and accumulating rate μ , while we prepare them at different, randomly selected initial potentials. In later studies, these condi-

tions need to be relaxed since in realistic biological neurons each neuron has different characteristics corresponding to its role in the brain functions [10,19]. The + sign in front of the coupling term in equation (3a) defines the “attracting” coupling dynamics. This term is used because positive coupling tends to reduce the differences between the interacting units: when u_i takes high values (higher than u_j) the coupling term becomes negative. This contribution tends to decrease the value of u_i (towards u_j) inhibiting its further growth. In the opposite case, when u_i takes lower values than u_j , the coupling term $[u_j - u_i]$ becomes positive and this contribution tends to increase the value of u_i , towards u_j .

Synchronization properties are quantitatively described by the mean phase velocity of each element $\omega_i = 2\pi c_i / \Delta T$, where c_i is the number of full cycles that element i has completed during the time interval ΔT [9]. Visually, synchronization patterns and chimera states are represented by color coded space-time plots that show the evolution of the oscillator potentials in time and space. These are particularly useful when transitions between different synchronization patterns take place, where the mean phase velocities do not give meaningful results. It is useful to introduce another quantitative index $\langle A(t) \rangle_t$, that represents the average ratio of elements below threshold. This will become clearer in Section 3 where states involving coexisting quasi-static and oscillatory elements will be discussed. The partially static profiles indicate that many elements are confined near the threshold, while a few escape towards the resting potential, $u_0 = 0$. The corresponding space-time plots reveal that these “active” elements are not localized and the activity propagates from one element to the next around the ring. In this case, the mean phase velocity is not an appropriate measure of coherence, because each element spends part of the time near the threshold and part of the time in the “active” state (performing excursions below threshold). The representative quantitative index $A(t)$ of the ratio of elements performing full cycles (from the rest state to the threshold) is, in general, time dependent and is defined as:

$$A(t) = \frac{1}{N} \sum_{i=1}^N q_i(t), \quad (4)$$

with

$$q_i(t) = \begin{cases} 1 & \text{when } u_i(t) \leq u_{th} - \theta \\ 0 & \text{otherwise,} \end{cases} \quad (5)$$

where θ takes small values. After the system has reached its steady state, the index $A(t)$ becomes statistically constant in time. Its time average $\langle A \rangle_t$ characterizes the activity in the system and will be referred to as “activity factor”.

Without loss of generality, throughout this work the parameters are fixed to values $\mu = 1.0$, $u_{th} = 0.98$, $u_0 = 0$, and the system size is $N = 1000$ elements.

3 Effects of nonlocal diffusive coupling

In the case of nonlocal connectivity of the LIF elements arranged in a ring geometry, the matrix σ_{ij} takes the form:

$$\sigma_{ij} = \begin{cases} \sigma & \text{for } i - R < j < i + R \\ 0 & \text{otherwise} \end{cases} \quad (6)$$

where σ is positive and all indices are understood as mod N . Each element i is linked with R other elements to its left and its right, thus the number of connections, $N_c = 2R$, is equal for all elements. The dimensionless coupling radius is defined as $r = R/N$ and represents the fraction of the system's constituents contributing to the dynamics of each element. In the next subsection we present the synchronization phenomena observed as we vary the coupling range r , the coupling strength σ and the refractory period p_r .

3.1 Variation of the coupling range

Using the nonlocal connectivity rules of equation (3), we simulate the LIF ring network and record the spatio-temporal evolution of the system.

Figure 1 presents typical snapshots and space-time plots of the system for different values of the coupling range R . We can see that oscillators organize into spatial clusters of elements remaining close to the threshold, interrupted by regions of oscillating nodes which make excursions away from the threshold. In most cases examined, the oscillating regions travel through the system with constant velocity. As the moving fronts on the right panels indicate, the velocity of the oscillating regions around the ring decreases as R increases.

As the coupling range R increases, the distribution of oscillating elements on the ring changes from many small to a few large active regions. This results in a smaller number N_a of active domains separated by an equal number N_{th} of near-threshold domains. If we denote by $\langle s_a \rangle$ and $\langle s_{th} \rangle$ the average size of active and near-threshold domains, respectively, the continuity condition around the ring is expressed by the following relation:

$$\langle N_{th} \rangle \langle s_{th} \rangle + \langle N_a \rangle \langle s_a \rangle = N, \quad (7)$$

where $N_a = N_{th}$. The size of the active and the near-threshold regions stay (statistically) constant in time. The oscillatory motion observed in Figures 1a–1d, i.e., a number of waves traveling at a constant velocity in a “sea” of almost static elements, is reminiscent of soliton propagation in a medium, although the condition for solitons are not exactly met in this system. The difference with soliton phenomena is apparent in Figure 1b, where the moving wave disappears while a new one is created in a nearby node. These patterns correspond to intermediate states which appear when the number of active (and near-threshold) domains changes, and will be discussed further in Section 3.2.

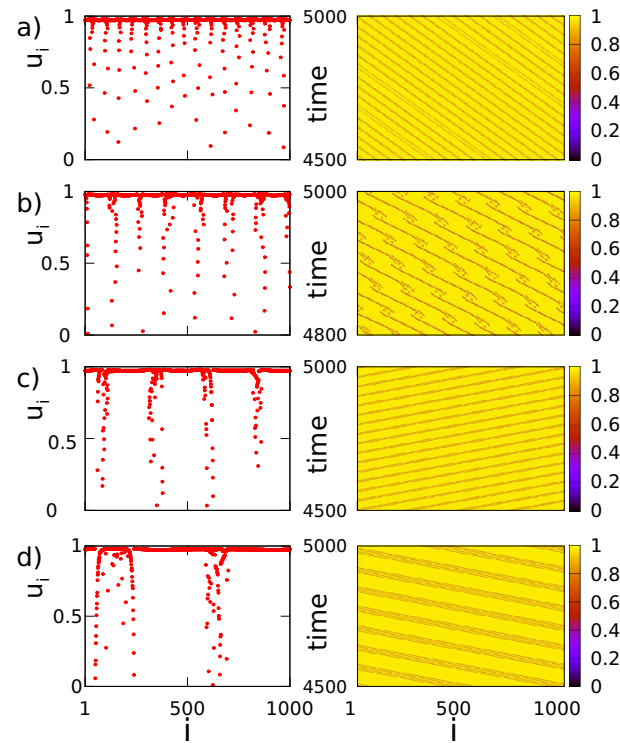


Fig. 1. LIF system with nonlocal connectivity: typical snapshots (left column) and space-time plots (right column). (a) $R = 50$, (b) $R = 100$, (c) $R = 200$, (d) $R = 350$. Other parameters are $p_r = 0$, $\sigma = 0.7$, $N = 1000$, $\mu = 1$, and $u_{th} = 0.98$. All realizations start from the same initial conditions, randomly chosen between 0 and u_{th} .

A counter-intuitive observation is that the number of active elements does not significantly depend on the coupling radius $r = R/N$. This can be seen in Figure 2, where the fraction of active elements is plotted as a function of r for three different values of the coupling constant σ . As r increases, the elements are redistributed into equidistant clusters (see Figs. 1b–1d), while the distance (in threshold elements) between active clusters increases. The quantity $\langle A \rangle_t$ is calculated as the time-average fraction of elements which have potential $u_i \leq 0.97$, i.e., $\theta = 0.01$. Average values and corresponding error bars are taken over 10 different initial conditions. In cases where the error bars are not visible, their size is smaller than the representing symbol. We observe that $\langle A \rangle_t$ stays constant, up to statistical fluctuations. This means that the magnitude of activity in the system mostly depends on the strength of the coupling. While the coupling strength σ is related to the magnitude of the activity, the coupling radius r is related to the organization of the activity in isolated regions and this might have important implications in the exchange of electrical signals between neurons.

3.2 Variation of the coupling strength

Modifications to the general activity of the system is also achieved with variations in the coupling constant σ .

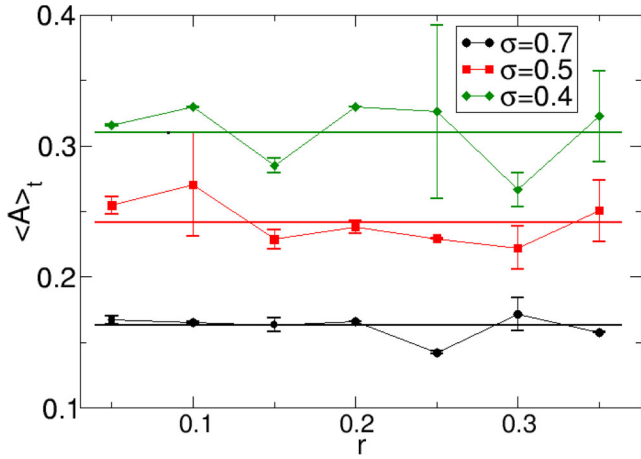


Fig. 2. The average activity factor $\langle A \rangle_t$ in the LIF system with diffusive nonlocal coupling as function of the coupling radius and for $\sigma = 0.7$ (black line) $\sigma = 0.5$ (red line) and $\sigma = 0.4$ (green line). Averages are taken over 10 initial conditions. The straight lines are guides to the eye. Other parameters as in Figure 1.

In Figure 3a, for small values of σ , we observe synchronized waves propagating through the system. As the coupling strength increases the oscillators organize into near-threshold clusters. These clusters are interrupted by elements making abrupt excursions towards the resting potential $u_0 = 0$ (Fig. 3b). While for small values of σ the oscillators follow one another keeping a constant phase difference (Figs. 3a and 3b), for large values of the coupling constant clusters are formed, which travel around the ring with a constant velocity (Fig. 3d). The transition from the synchronized waves to the clusters occurs for intermediate parameter values, around $\sigma \sim 0.6$ as depicted in Figure 3c.

In this case, a wave disappears but before vanishing, it coexists with another wave which has been spontaneously created at a nearby location. These hybrid states mediate (are at the turning point) between the simple moving waves and the clustered ones. As the parameter σ increases above 0.6, the regions of coexistence increase, gradually forming the clusters. These traveling clusters are separated again by near-threshold domains. The same effect was previously seen in Figure 1b, between the simple active clusters (Fig. 1a) and the composite (grouped) ones (Figs. 1c and 1d). For the working parameters used in Figure 1 the transition was recorded around $R = 100$, $\sigma = 0.7$, $p_r = 0$.

The activity factor $\langle A \rangle_t$ as a function of σ is shown in Figure 4. We observe a decrease in the number of active elements as the coupling strength grows. This can be intuitively understood as follows: the tendency of the oscillators to stay near the threshold is attributed to the exponential nature of the dynamics, which tends asymptotically to μ as $t \rightarrow \infty$. As σ increases, the system has the tendency to synchronize and therefore more and more elements are attracted to stay near the threshold. As seen from Figure 4, the value of the coupling radius r does not significantly modify the scaling of $\langle A \rangle_t$. This is in agree-

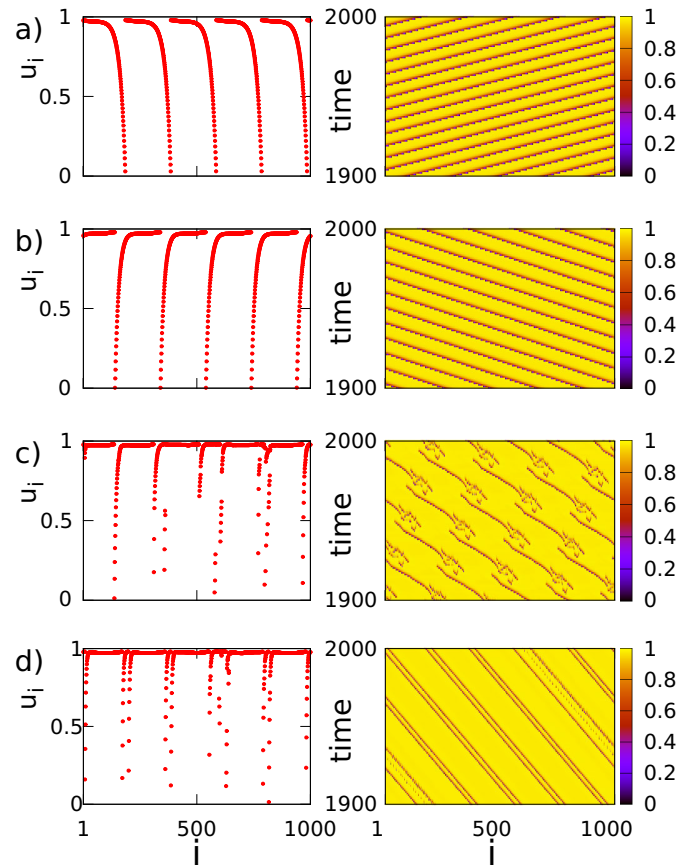


Fig. 3. LIF system with nonlocal connectivity: typical snapshots (left column) and space-time plots (right column). (a) $\sigma = 0.2$, (b) $\sigma = 0.3$, (c) $\sigma = 0.6$ and (d) $\sigma = 0.7$. Other parameters are $p_r = 0$, $R = 150$, $N = 1000$, $\mu = 1.0$ and $u_{th} = 0.98$.

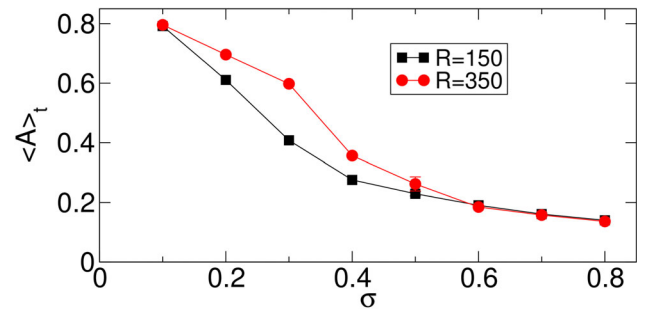


Fig. 4. The average activity factor $\langle A \rangle_t$ in the LIF system with diffusive nonlocal coupling as function of the coupling constant σ , for two different values of the coupling range $R = 150$ (black squares) and $R = 350$ (red circles). Other parameters as in Figure 1.

ment with Figure 2. We must note here that the splitting of the system in near-threshold and active domains is only observed in the case of attracting coupling. This phenomenon is not observed for repulsive coupling, where more classical chimeras are supported [37,38].

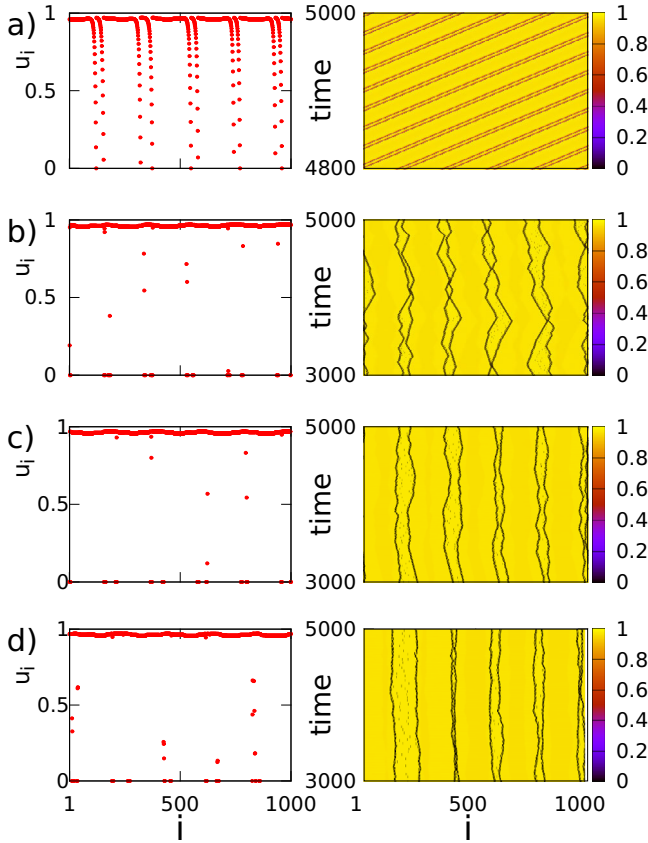


Fig. 5. LIF system with nonlocal connectivity: typical snapshots (left column) and space-time plots (right column). (a) $p_r = 0.01T_s$, (b) $p_r = 0.3T_s$, (c) $p_r = 0.5T_s$ and (d) $p_r = 0.8T_s$. Other parameters are $R = 150$, $\sigma = 0.7$, $N = 1000$, $\mu = 1.0$ and $u_{th} = 0.98$.

3.3 Variation of the refractory period

Similarly to Figures 1 and 3, Figure 5 displays snapshots and space-time plots for different values of the refractory period. For small values of p_r , Figure 5a shows clustering of active oscillators. As discussed previously in Sections 3.1 and 3.2, the clusters travel around the ring with a constant velocity, clearly indicated by the corresponding space-time plot. At the same time, all other elements take near-threshold values. As p_r increases, the ratio of below threshold elements $\langle A \rangle_t$ decreases, while the position of the clusters becomes pinned in space (see Figs. 5b and 5c). The activity is anchored around specific points of the ring, fluctuating locally around them. As p_r increases further, the fluctuations decrease and, as shown in Figure 5d, only specific elements make excursions away from the threshold. This decrease in the system activity is shown in Figure 6 where $\langle A \rangle_t$ is plotted as a function of p_r . Averages are taken over 10 different initial conditions. The refractory period induces a gradual, small decrease in the activity of the system, while pinning the position of the active elements. This effect has been verified for other values of r and σ (not shown).

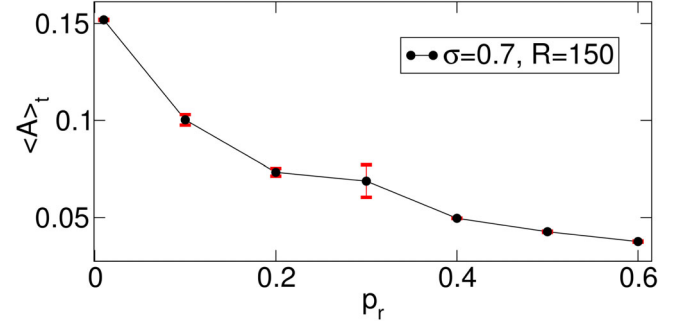


Fig. 6. The average activity factor $\langle A \rangle_t$ in the LIF system with diffusive nonlocal coupling as function of the refractory period p_r , for coupling range $R = 150$. Averages are taken over 10 initial conditions. Other parameters as in Figure 5.

4 Effects of reflecting coupling

The next step is to go beyond nonlocal symmetric coupling and examine more complex connectivities and their effect on the dynamics of the LIF network. Previous studies have shown that hierarchical connectivity, inspired by fMRI experiments, can give rise to complex phenomena such as “nested” and traveling multi-chimeras, as well as transitions between chimera states with different multiplicities [10,22,23,37,43]. In this study we introduce a new type of connectivity, the “mirror” or reflecting connectivity, which is motivated by the division of the brain in two symmetric hemispheres [32]. This means that elements belonging to one hemisphere can connect with elements in the other hemisphere and vice versa. In our simplistic model, where the LIF units are set on a ring architecture, we assume that each unit connects to its mirror image through a symmetry axis of the ring and to all the units belonging to a region of size R on the left and right of the mirror unit (see Fig. 7). Without loss of generality and due to the cyclic symmetry of our ring, we assume that the symmetry axis for the mirror images is the one that connects nodes $i = N$ (top) and $i = N/2$ (bottom), as marked in Figure 7. The reflecting connectivity matrix σ_{ij} linking node j to i takes the form:

$$\sigma_{ij} = \begin{cases} 1 & \text{for } N - i - R \leq j \leq N - i + R \\ 0 & \text{otherwise.} \end{cases} \quad (8)$$

Here, too, all indices are understood as mod N . The above connectivity form allows each LIF element to interact with the same, constant number of $2R$ elements with directed mirror links on the ring.

To investigate the effects of this connectivity scheme we first fix the number of links to $2R + 1 = 201$ ($R = 100$), and the refractory period to $p_r = 0$. The results are plotted in Figure 8, where alongside with the snapshots and space-time plots we show the mean phase velocity profiles.

Reflecting connectivity induces an unexpected phenomenon in the dynamics: for small values of the coupling constant $\sigma < 0.3$, the system is synchronized and the potential variables u_i of all oscillators cover the entire range $0 \leq u_i < u_{th}$ that is allowed from the system constraints

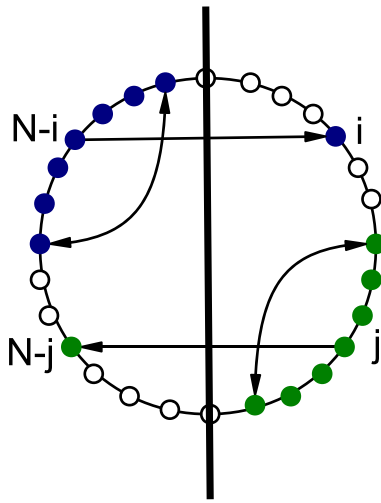


Fig. 7. Schematic representation of the mirror connectivity around the axis passing from elements set at positions N (top node) and $N/2$ (bottom node). The range of connectivity here is $R = 3$. For simplicity only the connectivity of element at position i on the top right (blue elements) and of element $N-j$ on the bottom left (green) are depicted. The connectivity of all other elements (including the white ones) is not shown.

(Eq. (1)). As σ increases, we observe a transition around the value $\sigma = 0.3$, where the elements on the one half-ring remain close to the threshold u_{th} , while the ones in the other half-ring oscillate between $[u_0, u_{th}]$ with varying mean phase velocities. We can say that this is a spatial coexistence of a coherent steady state domain and incoherent oscillations, because on one side the elements stay near threshold and on the other side they oscillate but their mean phase velocities present modulations that are more complex than in classical chimeras: as σ increases away from the transition, the oscillators in the middle of the active half-ring gradually develop a convex shape with a minimum in the middle of the active half-ring (Figs. 8c and 8d). While the maximum value of the mean phase velocity remains constant, the depth of the convex shape increases, as shown by Figure 8e, where the ω_{max} and ω_{min} values are depicted. As we increase further the coupling strength, a secondary ω peak develops in the middle of the active region (Fig. 8d), where the oscillators speed up with respect to their neighbors. For the chosen value of the coupling range, the size of the active region seems to remain almost constant as a function of σ . This is not always the case, as we show next.

Incoherent states with complex modulation in their mean phase velocities were previously observed in the FitzHugh-Nagumo model, where the single-headed chimeras transform into multi-chimeras whose multiplicity increases with the coupling radius r [9]. The difference with the current study is that here the chimera states coexist with a number of near-threshold oscillators and this is due to the combined effect of reflecting connectivity and positive (attracting) coupling dynamics. Another difference to reference [9] is that the modulations here take

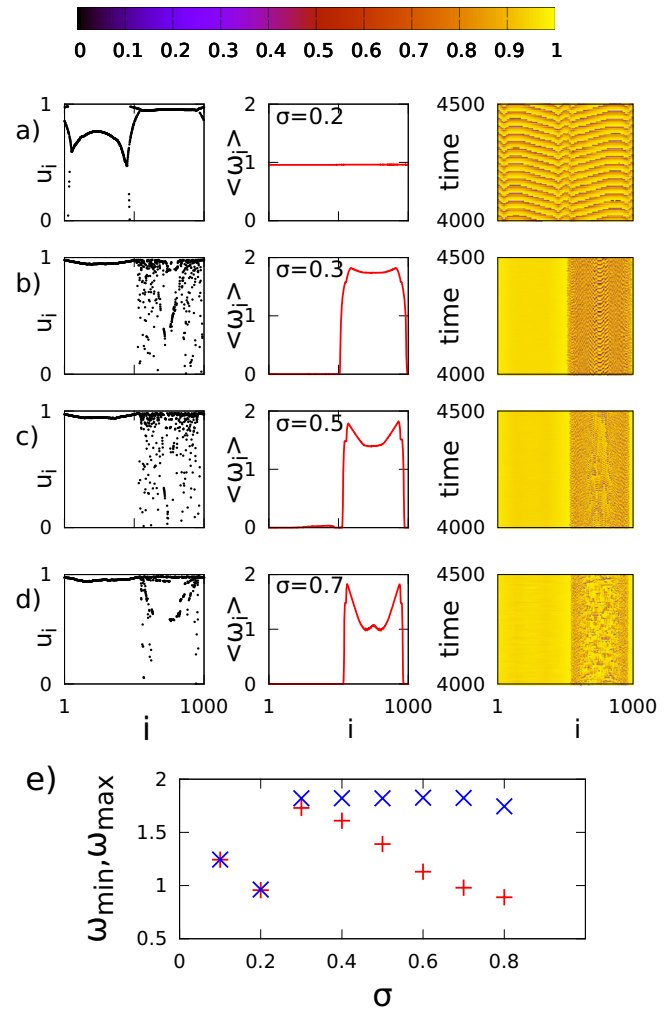


Fig. 8. LIF system with reflecting connectivity and varying coupling constant σ . Typical snapshots are depicted in the left column, mean phase velocities in the middle and space-time plots in the right column. (a) $\sigma = 0.2$, (b) $\sigma = 0.3$, (c) $\sigma = 0.5$, (d) $\sigma = 0.7$, (e) ω_{min} and ω_{max} as a function of σ . Other parameters are $N = 1000$, $R = 100$, $\mu = 1$ and $u_{th} = 0.98$ and $p_r = 0$. All realizations start from the same, randomly selected initial conditions between 0 and u_{th} .

place for large values of the coupling constant σ , after σ increases above certain values.

To further explore the influence of this connectivity on the system synchronization, we choose to examine the same features for a large value of coupling range, $R = 300$. Figure 9 shows that for small values of σ we have a synchronized regime, but around $\sigma = 0.2$ a first destabilization takes place when the system splits into two pairs of mutually synchronous regions. Around $\sigma = 0.3$ only one of the half-rings stays active, while in the other one the oscillator potentials stay near the threshold, u_{th} , and do not venture away from it. As before, near the threshold the mean phase velocity profile on the half-ring exhibits an arc-like shape, while as σ increases a plateau starts developing. For even larger values of σ , the convex shape

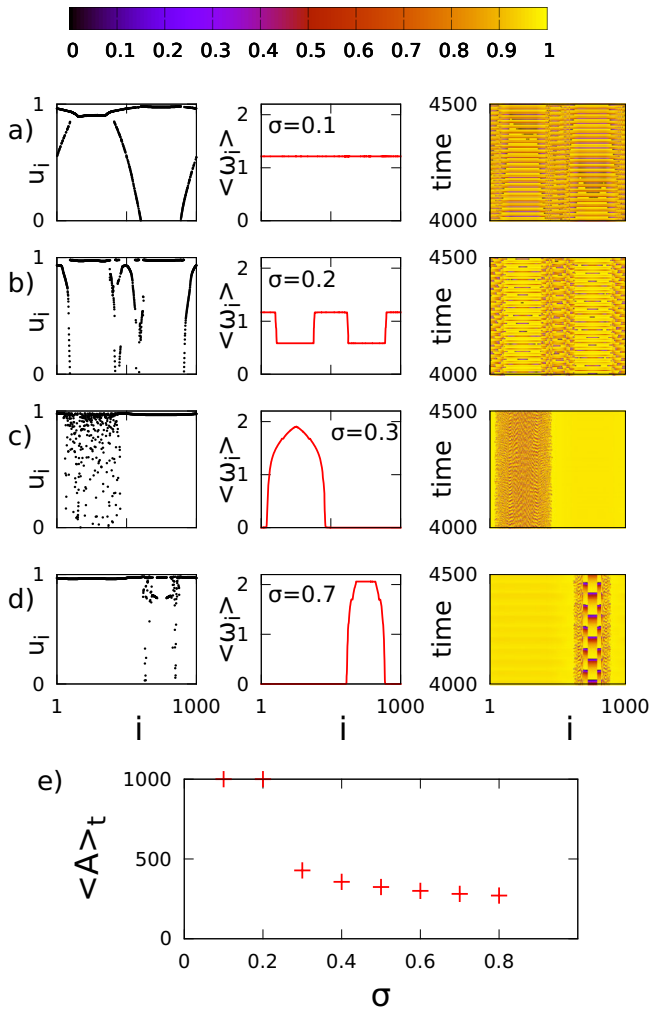


Fig. 9. LIF system with reflecting connectivity similar to Figure 8 and $R = 300$. (a) $\sigma = 0.2$, (b) $\sigma = 0.3$, (c) $\sigma = 0.5$, (d) $\sigma = 0.7$, (e) activity factor $\langle A \rangle_t$ as a function of σ . All other parameters as in Figure 8.

is formed in the middle of the active region (not shown). Comparison between Figures 9c and 9d indicates that the active region, shrinks with σ . Figure 9e depicts the activity $\langle A \rangle_t$ as a function of the coupling strength. For small coupling strengths all elements are active. Around $\sigma = 0.3$ a transition takes place and the active region is confined in one of the two half-rings. The active region shrinks further as σ increases.

Figures 8 and 9 indicate that the combined effects of attracting coupling together with reflecting connectivity induces a symmetry breaking in the system. When the coupling parameters increase above specific σ values the activity is confined to one half of the ring. For this choice of parameters the symmetry breaking takes place at values of σ between 0.2 and 0.3.

To prompt further into the properties of this system we study the dependence on the coupling range R , keeping the coupling strength constant, $\sigma = 0.4$ (other parameters as in the previous figures). In Figure 10 we can see

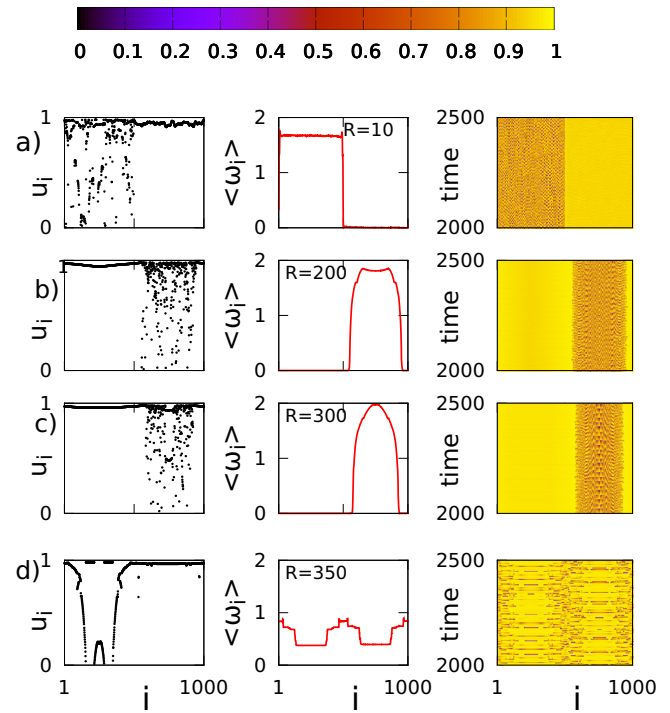


Fig. 10. LIF system with reflecting connectivity and varying coupling range R . Typical snapshots are depicted in the left column, mean phase velocities in the middle and space-time plots in the right column. (a) $R = 10$, (b) $R = 200$, (c) $R = 300$ and (d) $R = 350$. $\sigma = 0.4$, $p_r = 0$ and other parameters as in Figure 8.

that even for small R values, as small as 10, the activity is isolated into one of the two half-rings, with abrupt change of behavior at the interfaces. Counter-intuitively, as the coupling range increases, the width of the active stripe decreases up to a limit value of R , which for these parameter values is in the range $300 \leq R_{\text{lim}} \leq 350$. For large values of $R > R_{\text{lim}}$, the spreading of the coupling in larger regions causes oscillations in both parts of the system (Fig. 10d). The symmetry in the reflecting connectivity can be seen in the mean phase velocity plots: the oscillations in both half-rings are images of one another. Coherent oscillations are developed in the middle of each half-ring while the elements which border the half-ring connections are incoherent. As we further increase the coupling range, the incoherent regions shrink and the system synchronizes completely. In this respect, increasing the coupling range or the coupling constant causes different effects in the system: when the coupling range R increases the system passes from active-passive half-rings to active-active ones; when the coupling constant σ increases the system passes from the active-active phase to the active-passive one with simultaneous shrinking of the active phase.

Next we consider variations in the refractory period p_r , in Figure 11, keeping other parameters fixed to $R = 100$ and $\sigma = 0.4$. For $p_r = 0$ the system keeps the usual convex half-ring arrangement as was observed previously. As p_r

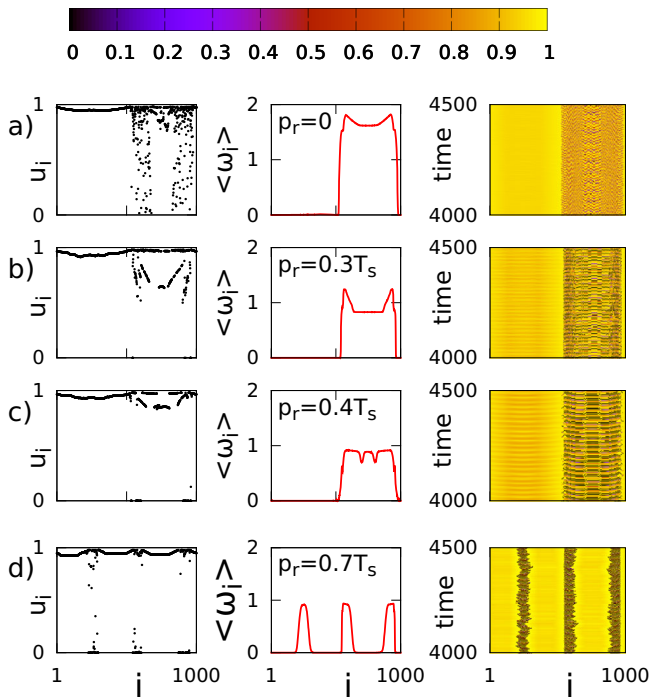


Fig. 11. LIF system with reflecting connectivity and varying refractory period p_r . Typical snapshots are depicted in the left column, mean phase velocities in the middle and space-time plots in the right column. (a) $p_r = 0$, (b) $p_r = 0.3T_s$, (c) $p_r = 0.4T_s$, and (d) $p_r = 0.7T_s$. $R = 100$, $\sigma = 0.4$ and other parameters as in Figure 8.

increases, the convex arrangement deepens, while around $p_r \sim 0.4T_s$ the mean phase velocity develops two minima of similar structure. This behavior persists for larger values of p_r , until around $p_r \sim 0.7T_s$ where a second transition takes place and the active domain splits into three smaller active ones which now reside in both half-rings. The introduction of the refractory period, therefore, induces multiple coherent and incoherent regions, separated by the near-threshold elements. These three regions are sustained for even larger values of p_r . Transient states (not shown) with two active stripes were observed but they were short-lived, turning either into single stripes or into the three stripes structure.

Finally, we take a closer look at the near-threshold elements. These elements are not entirely fixed, their potentials fluctuate near the threshold but they never make excursions to reach the resting state, u_0 . The size of the fluctuations away from u_{th} depends on the system parameters. Figure 12 shows details of the temporal behavior of the element $i = 35$ in the cases of $p_r = 0$, $0.1T_s$, $0.3T_s$ and $0.4T_s$, with all other parameters as in Figure 11. This figure provides evidence that the threshold elements fluctuate with higher amplitude as the refractory period increases.

Overall, the introduction of a reflecting connectivity induces a confinement of the oscillations in a single domain which resides in one half of the ring, while in the

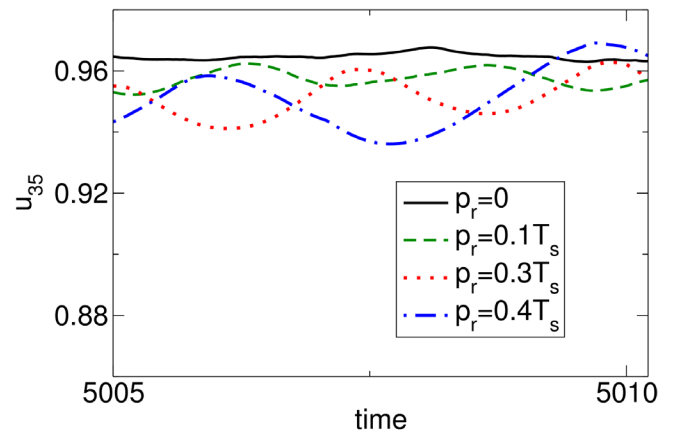


Fig. 12. Temporal evolution of the potential u of threshold LIF elements. Lines depict the fluctuations of element $i = 35$, for $p_r = 0$ (black, solid line), $p_r = 0.1T_s$ (green, dashed line), $p_r = 0.3T_s$ (red, dotted line) and $p_r = 0.4T_s$ (blue, dash-dotted line). $R = 100$, $\sigma = 0.4$ and other parameters as in Figure 11.

other half-ring the elements remain close to the threshold potential u_{th} . Within the active domains, the oscillators organize in regions with different mean phase velocities separated by transition regions. The introduction of a common refractory period in all LIF elements induces a splitting of the single active domain into smaller ones; these smaller active stripes reside in both half-rings.

5 Conclusions

Synchronization phenomena in diffusively coupled LIF elements were examined for nonlocal attracting coupling and for reflecting connectivity. In the case of the classical nonlocal diffusive coupling, traveling waves of synchronous elements with constant phase difference were observed, while chimera states were difficult to identify. Due to the traveling of the waves, all elements spend part of the time in the coherent domain and part in the incoherent one. Therefore, the difference in the mean phase velocities, which is the signature of the chimera states, smears out. It was numerically shown that the number of oscillators which are below the threshold is statistically constant in time and only depends on the parameter values σ and p_r .

In the case of reflecting connectivity, novel states involving incoherent domains coexisting with near threshold elements were found. This phenomenon is observed in the coupled model when each element is connected to its mirror units. For this connectivity, the oscillations are often restricted in one half of the ring, while the elements of the other half stay near the threshold. More specifically, for small values of the coupling constant σ the oscillatory activity covers the entire ring; as σ increases above a certain value, the activity is restricted in one of the half-rings while the size of the active region decreases inversely with σ . If a refractory period is added in the dynamics, the single activity regions split, while active regions

are spread in both half-rings, separated by near-threshold elements.

In the current study we assumed that all elements are identical. In future works it will be useful to assign different parameter values to the oscillators, taking into account their physiology and function. As a first approximation, one could add inhomogeneity in the form of a small dispersion around a mean value to any of the oscillator parameters, and study the implications of this statistical variation in the form and properties of the chimera states.

The above results find main applications in neuroscience where the complexity of the network topology and the nonlinearity of the neuron dynamics are confronted. It is widely believed that high connectivity is relevant in cognition, intelligence and creativity, while low or interrupted connectivity is related to mental disorders, such as schizophrenia, Alzheimer or Parkinson's disease [44,45]. The damage in the neurological disorders may be hereditary or develop with age. Therefore, it is very important to understand how this damage changes the network connectivity and consequently modifies the synchronization patterns. Thus, progress in the synchronization properties of network of oscillators will be important in the domain of neuroscience contributing in two ways: on the one hand the relation between neuron network architecture and brain functionality (perception and memory) will be elucidated, and on the other hand the association of connectivity with brain disorders will be unraveled. MRI and resting *vs.* task oriented fMRI experiments are expected to extract reliable brain connectivity patterns and to contribute highly in this research domain.

This work was supported by the German Academic Exchange Service (DAAD) and the Greek State Scholarship Foundation IKY within the PPP-IKYDA framework. Funding was also provided by NINDS R01-40596. P.H. and E.S. acknowledge support by DFG in the framework of the Collaborative Research Center 910. J.H. acknowledges support in the framework of the SIEMENS program "Establishing a Multidisciplinary and Effective Innovation and Entrepreneurship Hub". This work was supported by computational time granted from the Greek Research & Technology Network (GRNET) in the National HPC facility – ARIS – under Project ID PA002002.

Author contribution statement

N.D. Tsigkri-DeSmedt did the numerical simulations and data analysis. All authors designed the study and contributed in the preparation of the manuscript. All the authors have read and approved the final manuscript.

References

1. Y. Kuramoto, D. Battogtokh, *Nonlinear Phenom. Complex Syst.* **5**, 380 (2002)
2. D.M. Abrams, S.H. Strogatz, *Phys. Rev. Lett.* **93**, 174102 (2004)
3. M.J. Panaggio, D. Abrams, *Nonlinearity* **28**, R67 (2015)
4. E. Schöll, *Eur. Phys. J. Spec. Top.* **225**, 891 (2016)
5. C.R. Laing, C.C. Chow, *Neural Comput.* **13**, 1473 (2001)
6. H. Sakaguchi, *Phys. Rev. E* **73**, 031907 (2006)
7. I. Omelchenko, Y. Maistrenko, P. Hövel, E. Schöll, *Phys. Rev. Lett.* **106**, 234102 (2011)
8. J. Hizanidis, V. Kanas, A. Bezerianos, T. Bountis, *Int. J. Bifurc. Chaos* **24**, 1450030 (2014)
9. I. Omelchenko, O.E. Omel'chenko, P. Hövel, E. Schöll, *Phys. Rev. Lett.* **110**, 224101 (2013)
10. I. Omelchenko, A. Provata, J. Hizanidis, E. Schöll, P. Hövel, *Phys. Rev. E* **91**, 022917 (2015)
11. J. Hizanidis, N.E. Kouvaris, G. Zamora-López, A. Díaz-Guilera, C.G. Antonopoulos, *Sci. Rep.* **6**, 19845 (2016)
12. R.G. Andrzejak, C. Rummel, F. Mormann, K. Schindler, *Sci. Rep.* **6**, 23000 (2016)
13. N. Semenova, A. Zakharova, V. Anishchenko, E. Schöll, *Phys. Rev. Lett.* **117**, 014102 (2016)
14. A. Vüllings, J. Hizanidis, I. Omelchenko, P. Hövel, *New J. Phys.* **16**, 123039 (2014)
15. N. Brunel, M.C.W. Van Rossum, *Biol. Cybern.* **97**, 337 (2008)
16. A. Zakharova, M. Kapeller, E. Schöll, *Phys. Rev. Lett.* **112**, 154101 (2014)
17. I. Schneider, M. Kapeller, S. Loos, A. Zakharova, B. Fiedler, E. Schöll, *Phys. Rev. E* **92**, 052915 (2015)
18. T. Banerjee, *Europhys. Lett.* **110**, 60003 (2015)
19. S.A.M. Loos, J.C. Claussen, E. Schöll, A. Zakharova, *Phys. Rev. E* **93**, 012209 (2016)
20. T. Banerjee, P. Sharathi Dutta, A. Zakharova, E. Schöll, *Phys. Rev. E* **94**, 032206 (2016)
21. I. Omelchenko, O. Omel'chenko, A. Zakharova, M. Wolfrum, E. Schöll, *Phys. Rev. Lett.* **116**, 114101 (2016)
22. J. Hizanidis, E. Panagakou, I. Omelchenko, E. Schöll, P. Hövel, A. Provata, *Phys. Rev. E* **92**, 012915 (2015)
23. S. Ulonska, I. Omelchenko, A. Zakharova, E. Schöll, *Chaos* **26**, 094825 (2016)
24. O. Omel'chenko, M. Wolfrum, S. Yanchuk, Yu. Maistrenko, O. Sudakov, *Phys. Rev. E* **85**, 036210 (2012)
25. Y. Maistrenko, O. Sudakov, O. Osiv, V. Maistrenko, *New J. Phys.* **17**, 073037 (2015)
26. A. Schmidt, T. Kasimatis, J. Hizanidis, A. Provata, P. Hövel, *Phys. Rev. E* **95**, 032224 (2017)
27. R.A. Poldrack, M.J. Farah, *Nature* **526**, 371 (2015)
28. N.K. Logothetis, *Nature* **453**, 869 (2008)
29. P. Katsaloulis, D.A. Verganelakis, A. Provata, *Fractals* **17**, 181 (2009)
30. P. Expert, R. Lambiotte, D. Chialvo, K. Christensen, H.J. Jensen, D.J. Sharp, F. Turkheimer, *J. R. Soc. Interface* **8**, 472 (2011)
31. P. Katsaloulis, A. Ghosh, A.C. Philippe, A. Provata, R. Deriche, *Euro. Phys. J. B* **85**, 150 (2012)
32. E.S. Finn et al., *Nat. Neurosci.* **18**, 1664 (2015)
33. N.C. Rattenborg, C.J. Amlaner, S.L. Lima, *Neurosci. Biobehav. Rev.* **24**, 817 (2000)
34. N.C. Rattenborg, B. Voirin, S.M. Cruz, R. Tisdale, G. DellOmo, H.P. Lipp, M. Wikelski, A.L. Vyssotski, *Nat. Commun.* **7**, 12468 (2016)

35. S. Luccioli, A. Politi, Phys. Rev. Lett. **105**, 158104 (2010)
36. S. Olmi, A. Politi, A. Torcini, Europhys. Lett. **92**, 60007 (2010)
37. N.D. Tsigkri-DeSmedt, J. Hizanidis, P. Hövel, A. Provata, Proc. Comput. Sci. **66**, 13 (2015)
38. N.D. Tsigkri-DeSmedt, J. Hizanidis, P. Hövel, A. Provata, Euro. Phys. J., Special Topics **225**, 1149 (2016)
39. B. Ermentrout, Rep. Prog. Phys. **61**, 353 (1998)
40. R.D. Vilela, B. Lindner, Phys. Rev. E **80**, 031909 (2009)
41. B. Lindner, L. Schimansky-Geier, A. Longtin, Phys. Rev. E **66**, 031916 (2002)
42. N. Kouvaris, F. Müller, L. Schimansky-Geier, Phys. Rev. E **82**, 061124 (2010)
43. T. Isele, J. Hizanidis, A. Provata, P. Hövel, Phys. Rev. E **93**, 022217 (2016)
44. S. Ruiz, N. Birbaumer, R. Sitaram, Front. Psychiatry **4**, 17 (2013)
45. E. Hannon et al., Nat. Neurosci. **19**, 48 (2016)